J. Fluid Mech. (1978), *vol.* 89, *part* 3, *pp.* 469–495
Printed in Great Britain

Influence of wave dispersion on vortex pairing in a jet

By R. A. PETERSEN

Department of Aerospace Engineering, University of Southern California, Los Angeles†

(Received 15 September 1977 and in revised form 1 May 1978)

The geometry of large-scale structures in the turbulent mixing layer of a moderate Reynolds number jet is deduced from measurements of the fluctuating pressure in the hydrodynamic near field. The structures are rings of concentrated vorticity that distort with downstream distance until statistical axisymmetry disappears. The rings are spaced quasi-periodically and coalesce with each other, producing larger spacings. Statistical and flow-visualization techniques are applied to free and forced jets over a range of Reynolds numbers from 5000 to 50000 to demonstrate that rings of a given spacing do not coalesce with each other until they are far enough downstream that the local mixing layer has attained some critical thickness which scales with the wavelength of the vortex pair. Wave dispersion is evaluated as a plausible mechanism for localizing the coalescences. The central feature of the model is the observation that a shear layer is dispersive to wavelengths much longer than its thickness and non-dispersive to shorter waves.

1. Introduction

The notion that there is large-scale motion present in free shear layers is not new. The occurrence of spatially unstable waves in laminar shear flows was recognized in the last century. It has been known for at least twenty years that these waves roll up to produce cores of concentrated vorticity which eventually coalesce with each other to produce subharmonics. Anderson (1955) used flow visualization to observe pairings between vortex rings in a jet and Domm (1956) suggested vortex coalescence as the mechanism responsible for the production of subharmonics in two-dimensional mixing layers. Although these essentially periodic structures were considered to be low Reynolds number phenomena, Townsend (1956) at around this time anticipated the existence of large-scale motion within fully developed turbulent shear flows when he developed his eddy model.

The novel point of view that has emerged recently, chiefly from the flow-visualization experiments of Brown & Roshko (1971, 1974) and Winant & Browand (1974), is that the large-scale structures are *themselves* the mixing layers. From this perspective, shear-layer transition is related to the onset of nonlinearities in the large-scale motions. Coalescences between neighbouring concentrations of vorticity are primarily responsible for the linear spreading associated with turbulent shear layers. The three-dimensional mixing, which is the other property associated with turbulence, is, according to this view, either the result of the large momentum fluxes known to be

† Present address: Dynamics Technology, Inc., 3838 Carson Street, Torrance, California 90503.

associated with coalescences (Browand & Weidman 1976) or is caused by secondary instabilities intrinsic to the structures as suggested by Konrad, Roshko & Brown (1976).

If this concept is accurate, it is relevant to examine what factors influence the three-dimensional shape of the turbulent structures and to what extent their spacing and coalescence depend on local *vs.* initial conditions. This paper is motivated by these two questions and is confined to the cylindrical mixing layers of incompressible circular jets.

According to the model suggested by Laufer (1974), the organized structures in a turbulent jet are successive rings of concentrated vorticity. The arrangement is unstable to perturbations in the spacing between rings. The instability is axisymmetric and results in 'pairings' between adjacent rings. One can put foward purely kinematic arguments similar to those of Winant & Browand (1974) to show that the pairings are a sufficient mechanism for linear spreading. According to this model, the spacing between rings would increase exponentially with downstream distance. However, it is not clear whether the pairings are localized by the shear-layer dynamics or whether they are a purely kinematic process dependent only on initial conditions. The experimental evidence is inconclusive. Forcing experiments (Crow & Champagne 1971; Browand, Chu & Laufer 1975) indicate that initial conditions can affect global properties of the jet. On the other hand, free jet scaling suggests local dependence along the jet for coalescences between structures of a given spacing. For example, Laufer (1974) demonstrated that the local mean spacing between structures in a free jet scales with downstream distance over a wide range of exit Reynolds numbers. Since parallel stability theories (Michalke 1971; Mattingly & Chang 1974) show that the wavelength of the initial instability is determined by the initial shear-layer thickness, which depends on the exit Reynolds number, we must conclude that in a free jet the influence of the initial conditions has disappeared after the first few pairings. A plausible dynamic mechanism for local influence over coalescences is wave dispersion. The spatial stability analysis of Michalke (1971) indicates that a shear layer of a given thickness is dispersive to long waves and relatively non-dispersive to short waves. Generally speaking, the longest non-dispersive wave scales with the shear layer and has a theoretical wavelength of about eight shear-layer thicknesses (since $\omega\theta/U_e = 0{\cdot}1$ and $c_{\rm ph}/U_e = 0{\cdot}6$ from Michalke's figure 7, and since δ/θ is generally considered to be about 5). The vortex spacing $l(x)$ typically measured in turbulent jets (Laufer 1974) is

$$l(x)/D = 0{\cdot}55x/D$$

and the slope thickness is typically $\delta(x)/D = 0{\cdot}15x/D$. Consequently, the vortices are spaced about 3·5 shear-layer thicknesses apart, which makes the wavelength of the longest non-dispersive wave about twice the vortex spacing. Now, the large-scale vortex structures themselves are nonlinear, but the spatial perturbation that is necessary to initiate a pairing can be viewed as the superposition of a small amplitude subharmonic wave. It will be shown that the theoretical phase speed of the linear subharmonic is equal to the measured convection speed of the nonlinear vortex pair when coalescence occurs. By analogy with resonant interactions between long and short waves, we are suggesting that the small amplitude subharmonic needs to maintain a constant phase relative to the vortex pair in order for the coalescence to proceed. This model is consistent with the numerical observations of Patnaik, Sherman & Corcos

(1976). They simulated two-dimensional vortex coalescence in a non-dispersive mixing layer by allowing a vortex pair to interact with a subharmonic wave. They found that there are certain phase differences between the vortex pair and the subharmonic which effectively inhibit the coalescence.

Intrinsic to the physics of vortex coalescences in a jet is the question of the three-dimensional shape of the structures themselves. At very low exit Reynolds numbers (e.g. $U_eD/\nu = 5000$, where U_e = exit velocity and D = nozzle diameter) the structures are observed to be axisymmetric. However at higher Reynolds numbers there is strong experimental evidence suggesting that the structures become intermittently or predominantly helical. For example, in their flow-visualization studies, Browand & Laufer (1975) reported intermittent helical modes at Reynolds numbers greater than 15000. Similarly, modal-decomposition measurements by Fuchs (1974) at a much higher Reynolds number (400000) support the existence of higher-order azimuthal modes. The prevalence of helical concentrations of vorticity at high Reynolds numbers is disturbing for a couple of reasons. First, coalescences between helices would be more complicated geometrically, and would probably require a more complicated model. For example, Browand & Laufer (1975) suggested that such coalescences produce fractional subharmonics. Second, helical vortices introduce axial components of vorticity. Since there is no torque on the jet, there can be no vorticity normal to a convected fluid surface initiating from the nozzle exit plane. As the cylindrical vortex sheet rolls up to form a helical core, the fluid surface will have to strain in order to remain parallel with the core. The topology is difficult to visualize for an open structure like a helix. Since the existence of higher-order azimuthal modes raises such fundamental difficulties, experimental evidence is presented that suggests an alternative interpretation of previous observations, namely that mixing-layer structures remain ring-like at high Reynolds number, but that random straining gives the appearance of helices both visually and statistically.

The experimental apparatus and instrumentation are described in §2. The three-dimensional shape of the large-scale structures is explored experimentally at moderate Reynolds number in §3, and in §4 evidence is presented in support of the resonance model for vortex coalescence.

2. Apparatus

Two different jets were used for complementary parts of the study. A low speed air jet was used to deduce the geometry of the structures, while a water jet was convenient to study the effect of dispersion on vortex coalescence. Between them, the two sets of experiments encompassed a Reynolds number range of 5000–50000.

The air jet consisted of a stagnation chamber and a 2·54 cm diameter nozzle with a contraction ratio of 36:1. It was powered by a pump that permitted operating speeds of up to 60 m/s. The measurements reported here were performed at an exit velocity of 30 m/s, which corresponds to a Reynolds number of 52000 based on the exit diameter and velocity. The free shear layer was initially laminar at this speed, and the exit-plane turbulence level was measured at 0·003 U_e using a constant-temperature hot-wire anemometer. Most of the air-jet measurements were made in the hydrodynamic near field with $\frac{1}{8}$ in. diameter condenser microphones. The microphones were always positioned on a ray emanating from the edge of the nozzle which

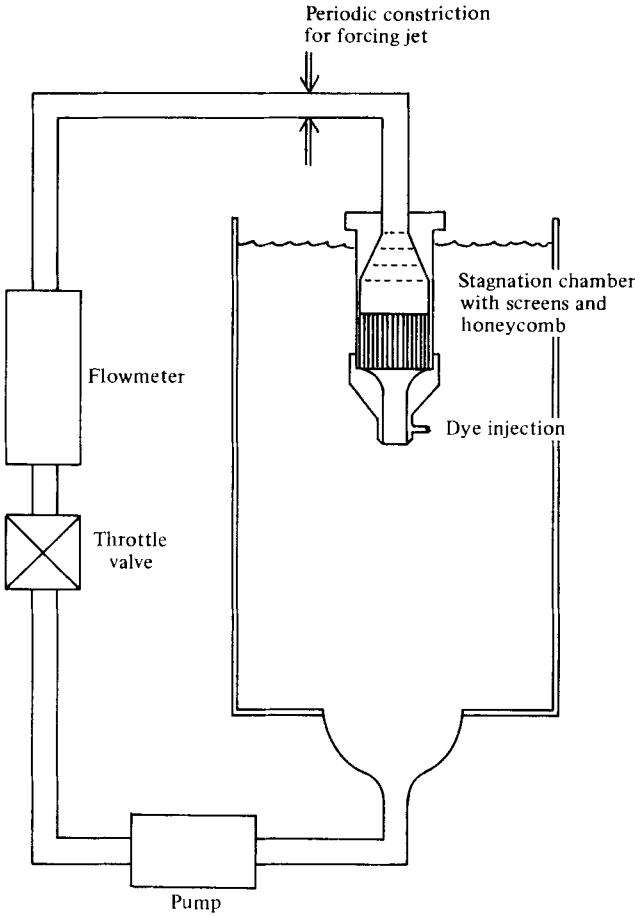

FIGURE 1. Water-jet facility.

made an angle of 10° with the jet axis. The planes of their diaphragms were parallel to the jet axis. When it was necessary to process the signals digitally, the analog records were sampled and digitized using a mini-computer subsystem of our own design.

The water-jet facility is shown schematically in figure 1. It was a closed system based on a centrifugal pump capable of providing 2·1 l/s against a head of 9·1 m of water. Throttling was provided by a gate valve. The stagnation chamber consisted of a conical inlet diffuser, a honeycomb flow straightener and a 3·81 cm diameter nozzle with a contraction ratio of 11:1. The maximum operating Reynolds number was 40000, which corresponds to an exit velocity of 1·4 m/s and a flow rate of 1·6 l/s. The jet was collected in an exhaust diffuser. The distance from the nozzle to the diffuser was approximately 20 diameters. Forcing of the jet was accomplished by periodically constricting the supply tube at a controlled frequency.

Flow visualization was made possible by injecting dye into the jet shear layer or by generating pulses of hydrogen bubbles at a wire stretched across the exit diameter. The dye used was red food colouring, which can be cleared by laundry bleach. The dye was injected into the nozzle boundary layer through a series of overlapping slots. The

flow rate of the dye was controlled such that the dye was concentrated into regions of high vorticity.

The hydrogen bubbles were generated from a 0·05 mm diameter platinum wire that was pulsed in excess of 40 V. The wire was chosen to be thin enough to give the desired quantity of bubbles, yet strong enough to withstand the jet mass flow. The pulse width generally selected was 10 % of the pulse period. To illuminate the bubbles it was necessary to backlight the jet using a vertical slit of light issuing towards the observer at an angle of 120°. The level of illumination was generally the minimum necessary for photography. To obtain proper exposures using strobed illumination, it was necessary to use 10–15 s exposures and to push the film to an ASA of about 3000.

3. Shape and spacing of coherent mixing-layer structures

The use of a passive contaminant such as dye is useful for visualizing concentrations of vorticity in low Reynolds number jets. At high Reynolds numbers, the increased mixing disperses the contaminant, making this a difficult and unreliable technique. An alternative technique, introduced by Mollo-Christensen (1967), is to measure near-field static-pressure fluctuations. Static-pressure fluctuations in the hydrodynamic near field of an incompressible shear layer are induced by velocity fluctuations inside the layer. The consequent spatial averaging makes the near field particularly sensitive to coherent motion buried within the turbulence. The phase relationship between the induced pressure and velocity fields of the coherent structures has been mapped out for a jet mixing layer by Lau, Fisher & Fuchs (1972).

The static-pressure measurements were made outside the air jet using condenser microphones located at the 'edge' of the flow, where the intermittency was small. The jet was operated at a Reynolds number of 50000. When microphones are used to measure static-pressure fluctuations there is always the question of velocity contamination. Work by Siddon (1969) and by Fuchs (1972) indicates that velocity contamination can be effectively eliminated by proper design of a microphone fairing. In the present investigation the microphones were operated without aerodynamic fairings so there was probably some contamination, particularly from induced radial velocity fluctuations. Some contamination was considered acceptable for the purposes of this investigation so long as the microphones responded in a consistent way to the passage of discrete structures.

3.1. *Near-field convection measurements*

In order to establish whether the microphones were responding to the mixing-layer structures, space–time correlations were measured between microphones. Measured estimates of the convection speed and spacing of the structures were compared with independent investigations.

The mean convection speed of the structures was estimated by cross-correlating the signals from two microphones separated axially. The normalized cross-correlations are shown in figure 2 for various downstream positions along a cone of half-angle 10°. The axial location refers to the upstream microphone, the separation between the microphones was 5·0 mm, and the time delay corresponding to the cross-correlation peak was assumed to be the average time for the structures to travel between microphones. The mean convection speeds, defined as separation distance divided by

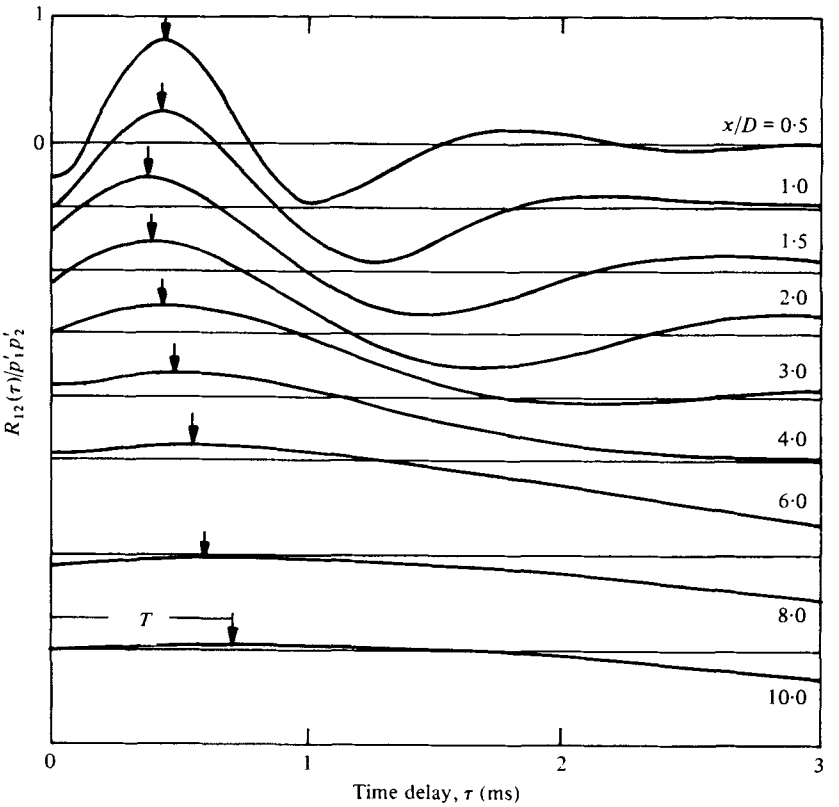

FIGURE 2. Cross-correlation coefficients between two near-field microphones. Separation ξ/D = 0·20, convection time = T. The location x/D refers to the upstream microphone.

convection time, appear in figure 3 as a function of downstream position. The broadening of the cross-correlation peaks with downstream location evident in figure 2 was responsible for the increasing uncertainty in the estimates of the convection speed beyond three or four diameters. The convection speeds were normalized by the jet exit speed, and the ratios are in good agreement with previous investigations. Downstream of the potential core the convection speed decayed asymptotically as $1/x$, and was about half the local centre-line speed.

Normalized autocorrelations measured at the same downstream positions are shown in figure 4. Along the potential core ($x/D \leqslant 4$) the autocorrelations were periodic and the time scale indicated in the figure reflects the mean periodicity of the discrete structures. Beyond the potential core the autocorrelations became aperiodic. In the range $4 < x/D < 7$ there was no spectral peak at all. Beyond 7 diameters, although the autocorrelations remained aperiodic they did exhibit a correlation minimum. For consistency, the minimum was used to define a time scale. However these time scales should not be interpreted as periods. The estimated spacing between structures, based on the measured periodicity and convection speed, increases roughly linearly with downstream distance in keeping with the spreading of the mixing layer. These measurements of mean spacing have been previously reported by Laufer, Kaplan & Chu (1974, figure 3) and agree with the results of independent investigators.

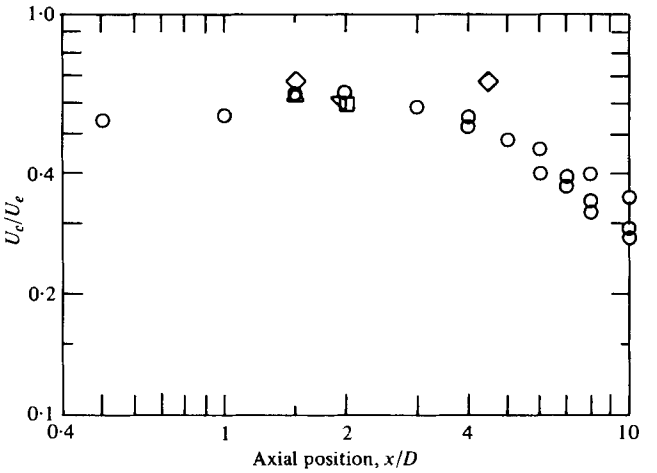

FIGURE 3. Mean turbulent convection speed. ○, present data; □, Lau *et al.* (1972); △, Ko & Davies (1971); ◇, Davies, Fisher & Barratt (1963); ▽, Bradshaw, Ferriss & Johnson (1964).

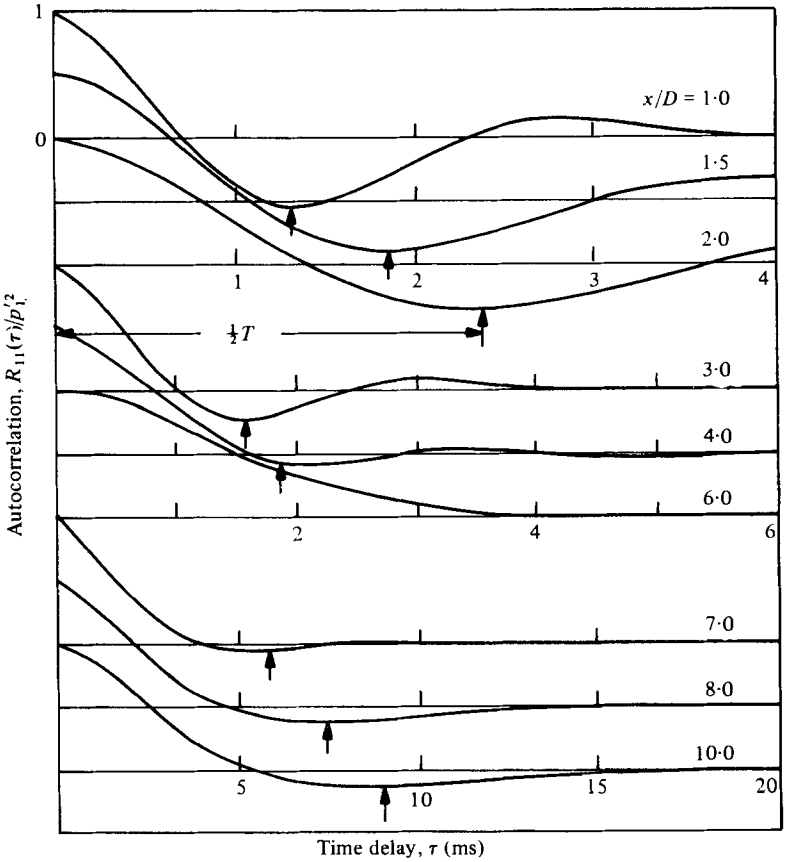

FIGURE 4. Near-field autocorrelation coefficients. Microphones were positioned along a cone of half-angle 10°. Time T is period of passage.

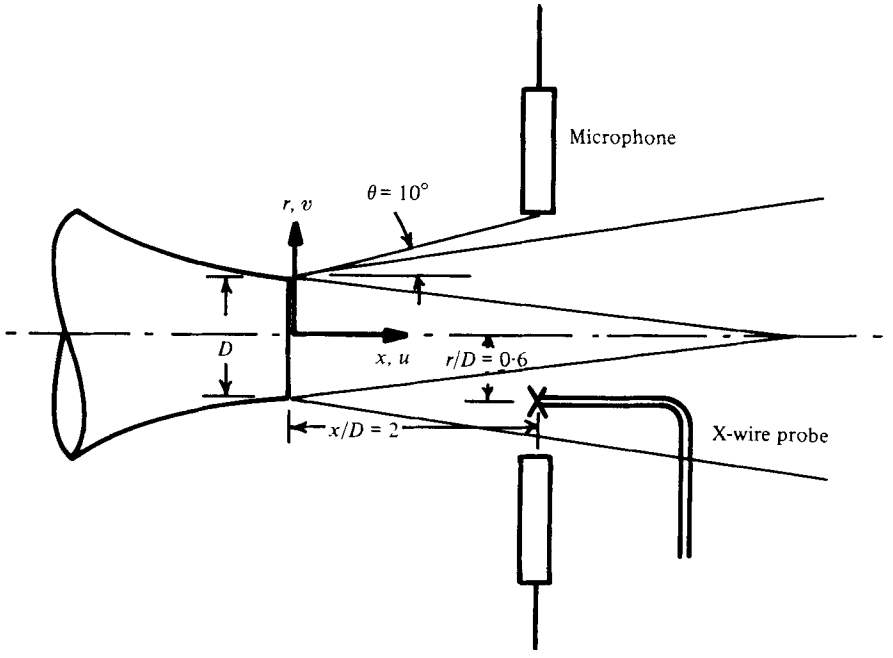

FIGURE 5. Experimental arrangement for mixing-layer eduction conditioned on near-field microphone signature.

3.2. *Phase relation between coherent structures and near-field microphone signal*

That the convection speed and spacing of the structures as measured by the microphones exhibit the correct scaling with downstream distance indicates that the microphones responded to the passage of the coherent structures. The phase relationship between the structures and the microphone signal was then determined by conditional sampling of the turbulent velocity recorded from an X-wire probe located inside the mixing layer. The sampling condition was generated from two microphones located in the near field of the jet. The experimental arrangement is indicated in figure 5. The X-wire probe was located inside the mixing layer at the position $r/D = 0{\cdot}6$, $x/D = 2$, while the microphones were located at the outer edge of the jet on a cone of half-angle 10°. One of the microphones was located at the azimuthal angle of the probe, while the other was diametrically opposite. The X-wires were oriented to decompose the turbulence into radial and axial components. The turbulence was sampled whenever both microphone signals passed through zero simultaneously and with slopes of the same sign. This sampling condition provided a precise time reference and selected structures that were axisymmetric. The results of the conditional sampling are shown in figure 6. The upper two traces are the fluctuating axial and radial velocity components, while the middle trace, the unsteady momentum flux, is the product of the two components normalized by their respective r.m.s. values. The lower two traces are the pressure signals of the microphones located adjacent to the probe ($\phi = 0$) and diametrically opposite ($\phi = \pi$). The vertical scale is in half r.m.s. intervals. The velocity record was sampled whenever the two microphone signals simultaneously passed through zero with positive slope. The time axis

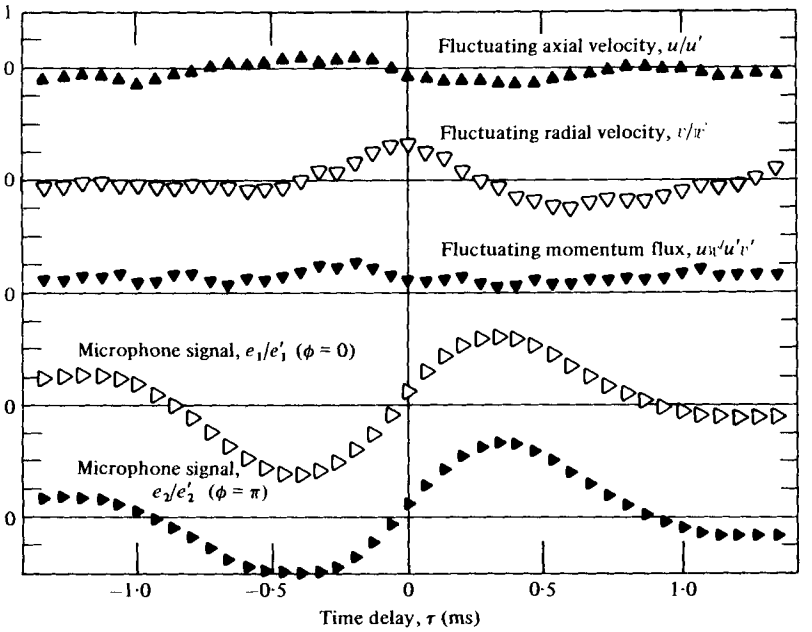

FIGURE 6. Educed turbulent velocities conditioned on simultaneous near-field zero crossings with positive slopes.

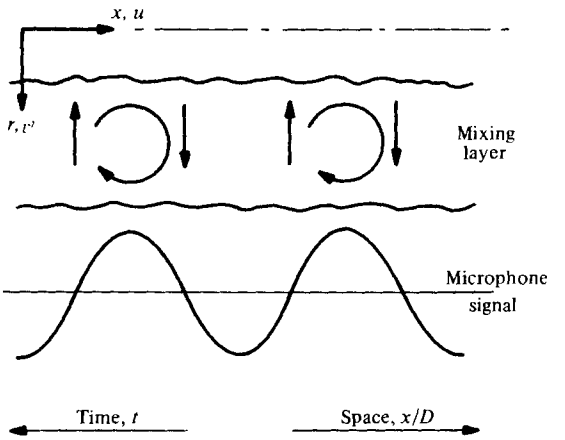

FIGURE 7. Inferred phase relationship between vortex cores and near-field microphone signal.

represents positive and negative delayed time with respect to the sampling conditions. The signatures shown on the figure are the resulting conditional average over an ensemble of 100 individual samples. From the figure it is apparent that the sampling conditions were not effective in educing information about the axial velocity or momentum flux. However, the sampling conditions did educe a significant radial velocity signature. A positive radial velocity peak preceded a positive peak in the microphone signals by a quarter-wave. When this phase relationship is visualized in the spatial domain (figure 7) it follows from the sign of the mean vorticity that the

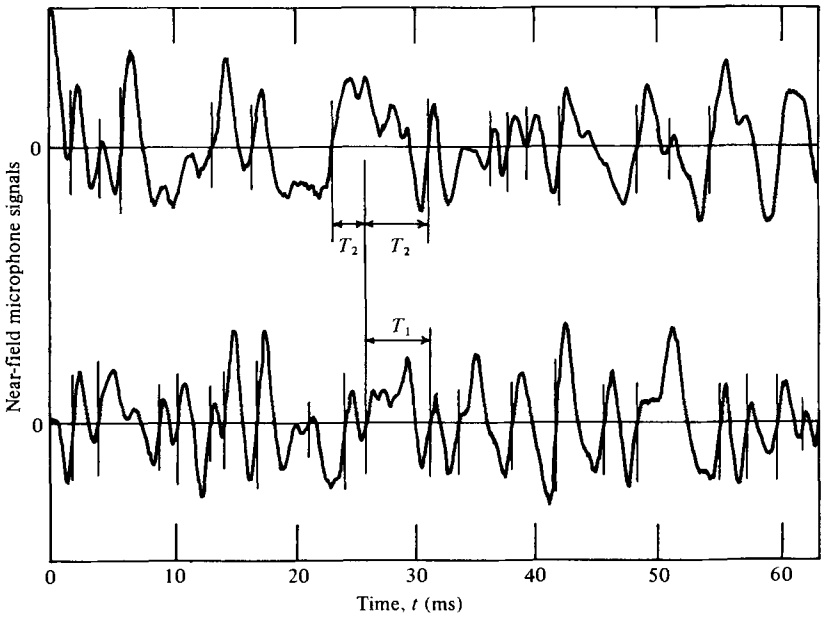

FIGURE 8. Definitions of zero crossing intervals T_1 and T_2 superimposed on sample records of two diametrically opposite microphones.

ring vortex was in phase with positive peaks in the microphone signal. Since the capacitor microphones used in the experiment inverted the signal, the positive peak probably corresponds to a negative static-pressure fluctuation, which would agree with Lau *et al.* (1972).

The inability of the sampling conditions to educe significant axial velocity signatures is probably due to radial variations between successive vortices. Since the X-wire probe was located near the centre of the mixing layer, the centre of vorticity would be equally likely to pass above the probe as below. It should be emphasized that axisymmetry was built into the sampling condition. The condition was rarely satisfied and the resulting ensemble average represents only about 10% of the data record. When the conditional sampling was repeated, but this time conditioned on zero crossings in the signal of a single microphone, the condition was insufficient to educe a significant signature in even the radial velocity. So it appears that there are significant departures from axisymmetry for a significant fraction of the time.

3.3. *Zero-crossing statistics*

At this point it is appropriate to separate the question of axisymmetry from the question of topology. For example, the near field of randomly oriented vortex rings can be decomposed statistically into higher-order azimuthal modes. However they would still be ring-shaped and would, for example, generate subharmonics differently than would helically shaped-vortices.

Whether the structures are typically ring shaped or helical was investigated statistically from their near-field signatures by noting zero crossings in the records of a microphone pair located on opposite sides of the jet and by generating appropriate probability densities. The concept is indicated in figure 8. Microphones were placed

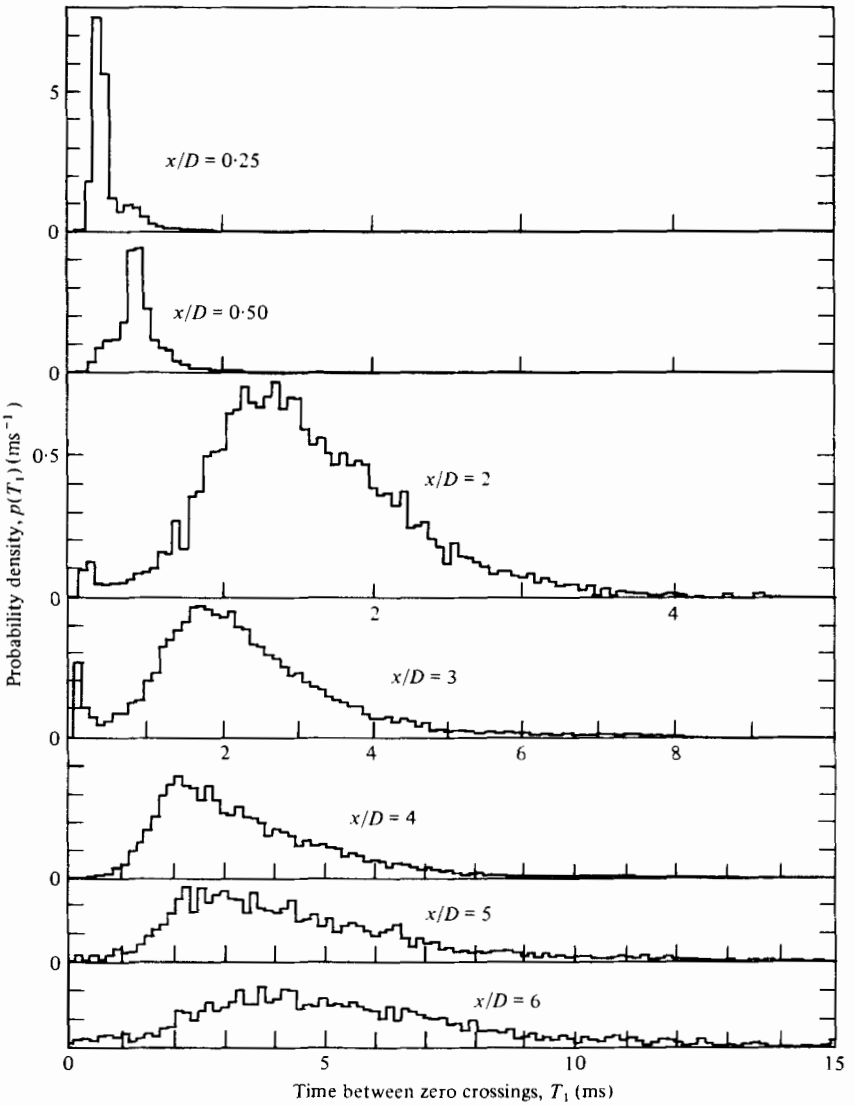

FIGURE 9. Probability distributions of time T_1, the interval between adjacent zero crossings.

in the near field on either side of the jet, each signal was digitized and the digital record was marked whenever it crossed zero with positive slope. The time T_1 was the interval between successive zero crossings in the same microphone signal and the time T_2 the interval between successive zero crossings in the signals from opposite microphones. From these intervals, probability densities $p(T_1)$ and $p(T_2)$ were generated.

Unlike space–time correlations, the zero-crossing statistics characterize the record as a series of discrete events rather than as a superposition of harmonic waves. If the signal was periodic, the single-channel probability density, for example, would consist of a single delta function located at the period of the wave. Similarly if the structures

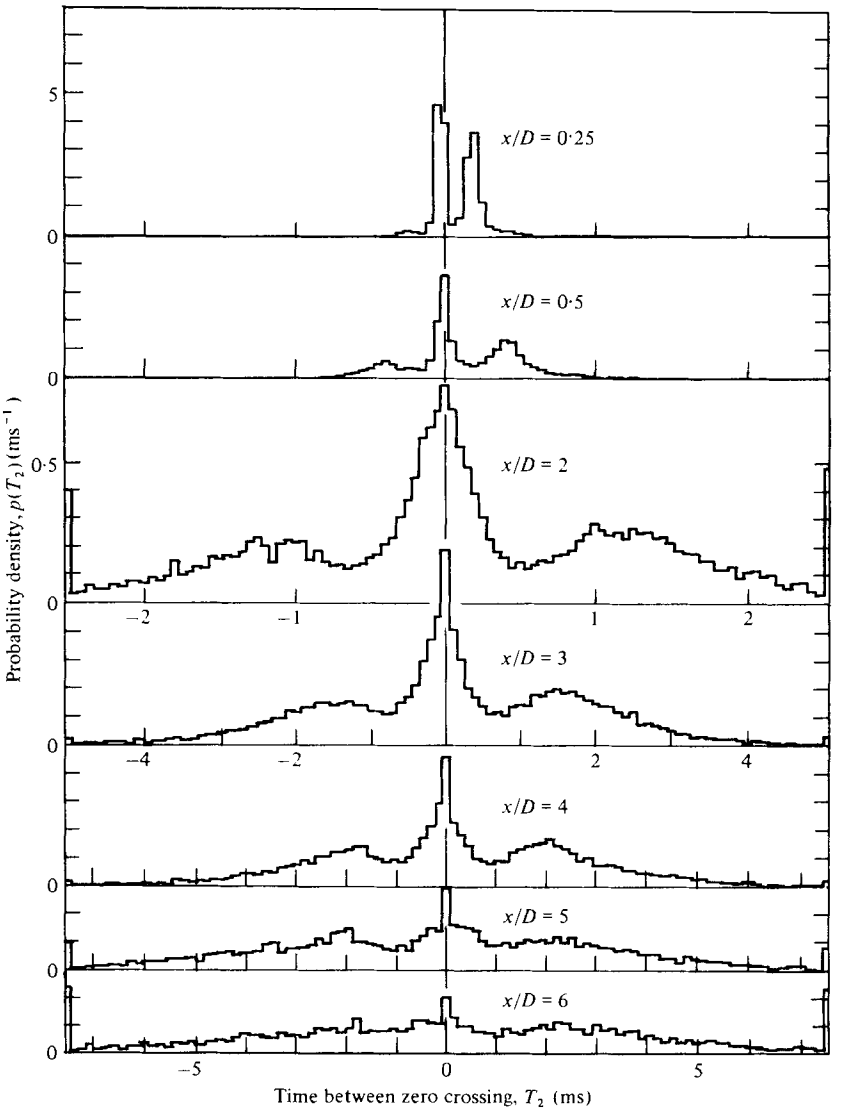

FIGURE 10. Probability distribution of time T_2, the interval between zero crossings on opposite sides of the jet.

were ring shaped the cross-channel probability densities would be expected to exhibit side peaks at time intervals of plus and minus one period. Any randomness in the spacing or orientation of the rings would result in broadening of the side peaks. Should the structures be helical for a significant fraction of the time, the cross-channel probability densities would be expected to exhibit a second set of side peaks at time intervals of plus and minus a half-period.

The single-channel statistics $p(T_1)$ are summarized in figure 9 and the cross-channel statistics $p(T_2)$ appear in figure 10. Each figure shows a family of probability densities corresponding to different axial positions between $x/D = 0{\cdot}25$ and 6. In each figure the abscissa is the interval in ms between zero crossings. The ability

of these techniques to separate time scales is illustrated in figure 9 for $x/D = 3$. The narrow peak on the left side of the probability density was caused by high frequency amplifier noise. It has been separated from the time scales associated with the turbulence. Within the first four diameters, the single-channel statistics generally exhibited a single probability peak, whereas the cross-channel statistics exhibited a central maximum at $T_z = 0$ and also secondary maxima equally spaced at positive and negative time intervals. In each case the time interval associated with the secondary maxima was the most probable interval based on the single-channel statistics. So, whenever an event with the characteristic time scale was observed on one side of the jet, it appeared on the other side either simultaneously or delayed by plus or minus one period. By implication, the mixing-layer structures were ring shaped at least within the potential-core region and exhibited some degree of randomness in spacing and/or orientation.

Beyond the potential-core region of the jet ($x/D = 5$ and 6), the secondary peaks in the cross probability densities broadened and the central peak diminished, suggesting large departures from axisymmetry and periodicity. This is in qualitative agreement with the near-field autocorrelations (figure 4). The raggedness in the zero-crossing statistics at these locations was due to the small data base.

The occurrence of a vortex pairing is evident in the single-channel statistics (figure 9). At the location $x/D = 0{\cdot}25$ the probability peak occurred in the range 200–250 μs (50 μs was the sampling resolution), corresponding to the eigenmode ($St = 3{\cdot}7$). However, there was a secondary peak in the range 450–500 μs, double the eigenmode period. By $x/D = 0{\cdot}5$, the probability peak shifted to the subharmonic, with a secondary peak at the eigenmode period. Such a discrete shift in time scale to a subharmonic is characteristic of a pairing. The cross probability densities were skewed at these early axial locations owing to slight misalignment of the microphones. Further downstream ($x/D \geqslant 2$), the probability peak exhibited a continuous shift towards longer time scales. We feel that there were still pairings at these locations, but that their occurrence was random over an increasingly large spatial region.

3.4. *Summary of time scales*

Two physically meaningful time scales can be derived from the single-channel zero-crossing statistics: the most probable spacing between zero crossings and the expected or mean spacing. The two time scales are normalized as Strouhal numbers D/TU_e and plotted against downstream distance in figure 11. As would be expected, the most probable Strouhal number was consistently larger than the Strouhal number based on the mean spacing. Strouhal numbers based on the autocorrelation time scale (figure 4) and on the power spectral peak are also plotted for comparison. Although they were obtained from the same data base the spread was as much as an octave with the autocorrelation Strouhal numbers intermediate between the mean and most probable Strouhal numbers and with the spectral-peak Strouhal numbers the smallest of the group.

Measurements by other investigators shown in the figure indicate that, even though there is a spread of as much as an octave between different types of time scale, a consistent definition will produce consistent scaling, independent of the Reynolds number or Mach number. For example, the time scales reported by Ko & Davies

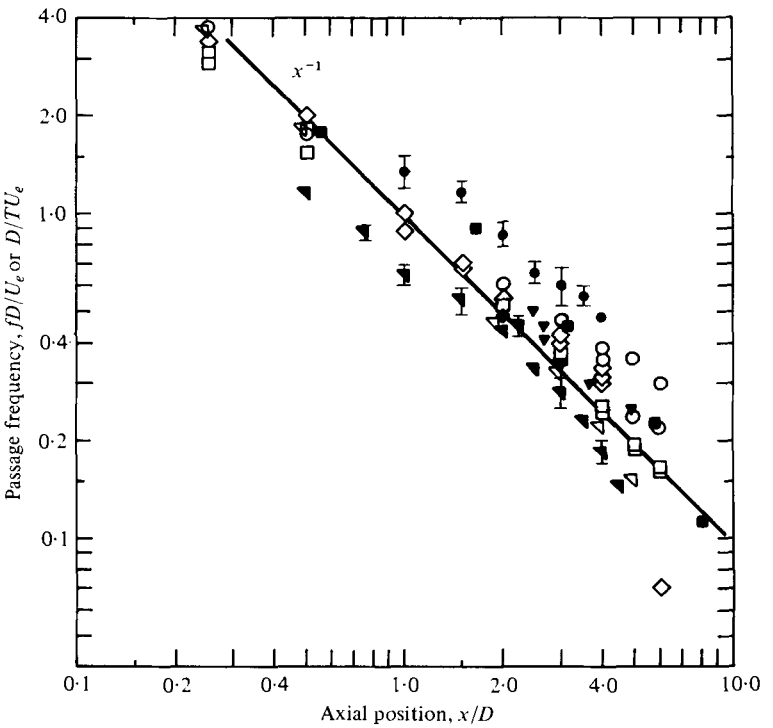

FIGURE 11. Summary of turbulent jet time scales, based on a variety of measurement techniques. Present data: ○, most probable passage period (zero-crossing statistics); □, mean passage period (zero-crossing statistics); ◇, correlation period; ◹, spectral peak. ◆, Lau *et al.* (1972); ●, Browand *et al.* (1975); ■, Michalke & Fuchs (1975); ▼, Crow & Champagne (1971); ◥, Ko & Davies (1971).

(1971) were derived from spectral peaks obtained for a comparatively high Reynolds number jet and scale with the spectral peak Strouhal numbers reported here. Similarly a correlation time scale (Lau *et al.* 1972) scales with the corresponding time scale reported here. The exceptions are the time scales reported by Browand *et al.* (1975), which were derived from dye-visualization motion pictures of a low Reynolds number water jet. Their Strouhal numbers are generally larger than any of the present measurements. It is not clear whether this is due to their rather small data base or whether some vortex structures are being missed with present methods.

3.5. *Azimuthal array of microphones*

In order to ensure that the various statistical measurements were being interpreted reasonably, an azimuthal array of nine microphones was constructed to visualize the structures. The microphones were equally spaced on a semicircular arc that formed the base of a 10° half-angle cone with apex inside the nozzle exit. Data were recorded at downstream distances of 2, 4 and 6 diameters. The signals were converted to digital records (effective sampling rate = 20 kHz), high-pass filtered above 50 Hz and normalized by their individual r.m.s. levels.

A brief sample of the data collected at $x/D = 6$ appears in figure 12. The nine traces represent simultaneous records from the nine microphones, which were equally spaced

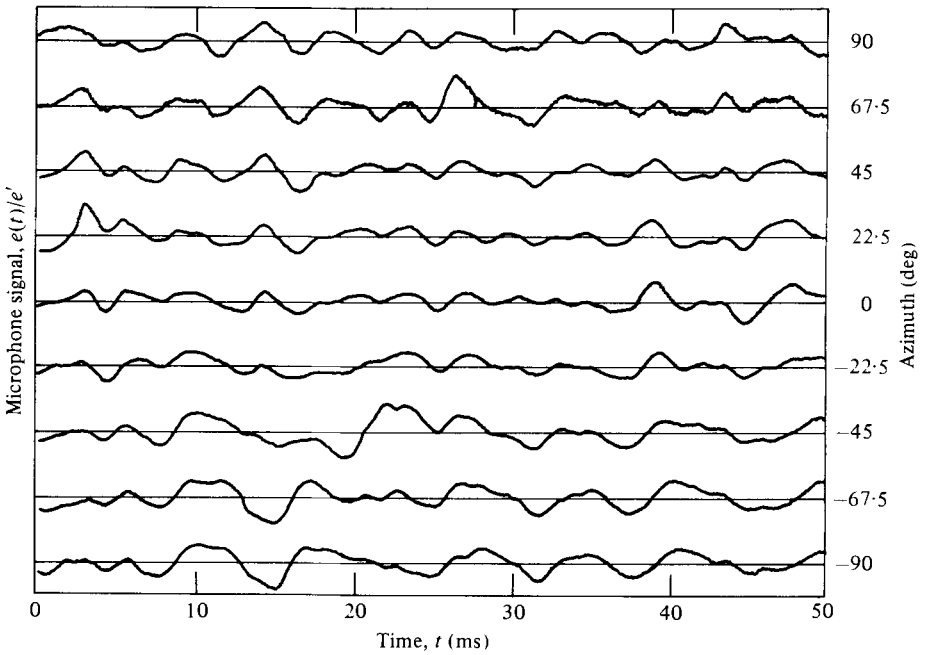

FIGURE 12. Near-field azimuthal pressure records. Nine microphones equally spaced azimuthally on a 10° half-angle cone and positioned six diameters downstream.

azimuthally 22·5° apart. Although there was considerable continuity from one microphone to the next, it is hard to judge the degree of axisymmetry from this type of display. To improve the visualization the oblique projections shown in figure 13 were adopted. Each microphone record was projected at an angle corresponding to its azimuth about the jet. The radius vector $\mathbf{r}_\phi(t)$ corresponding to each trace is a function of time and consists of an unsteady part, proportional to the microphone signal, superimposed on the jet radius. That is,

$$r_\phi(t) = R[1 + 0{\cdot}1\, p_\phi(t)/p'_\phi],$$

where R is the jet radius and $p_\phi(t)$ is the signal from the microphone with azimuth ϕ from the vertical. The factor 0·1 provided the best visualization and has no physical significance. The radius vector was projected according to the transform

$$\begin{bmatrix} X_\phi \\ Y_\phi \end{bmatrix}(t) = \begin{bmatrix} 1 & -\frac{1}{2}\sin\phi \\ 0 & \cos\phi \end{bmatrix} \begin{bmatrix} U_c t \\ r_\phi(t) \end{bmatrix},$$

where U_c, the convection speed of the structures, was selected as $0{\cdot}6U_e$. The dimensions X_ϕ and Y_ϕ were normalized by the jet diameter D, so that the 'time' axis is expressed in convected diameters. This type of display preserves the correct spatial proportions of the jet, making the azimuthal shape of the structure easier to visualize. However the display is only a visualization technique and does not, for example, describe the motion of the jet interface.

The sequence of visualizations at the downstream locations $x/D = 2$, 4 and 6 complements the conditional zero-crossing statistics. At $x/D = 2$, the structures were circumferentially coherent rings. Although the rings were clearly axisymmetric in a

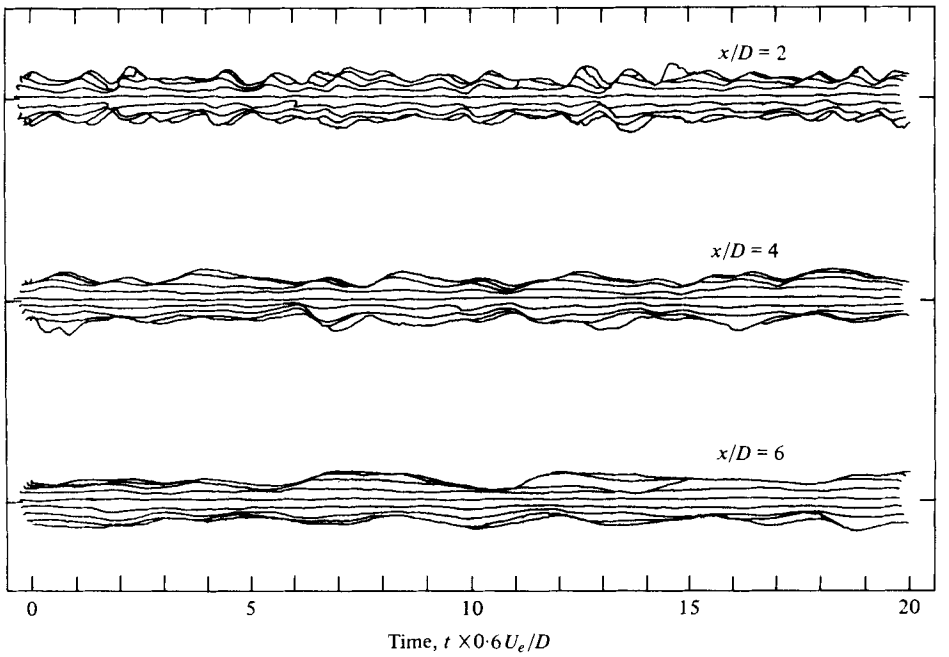

FIGURE 13. Azimuthal pressure records: oblique projections with the time axis expressed in convected diameters.

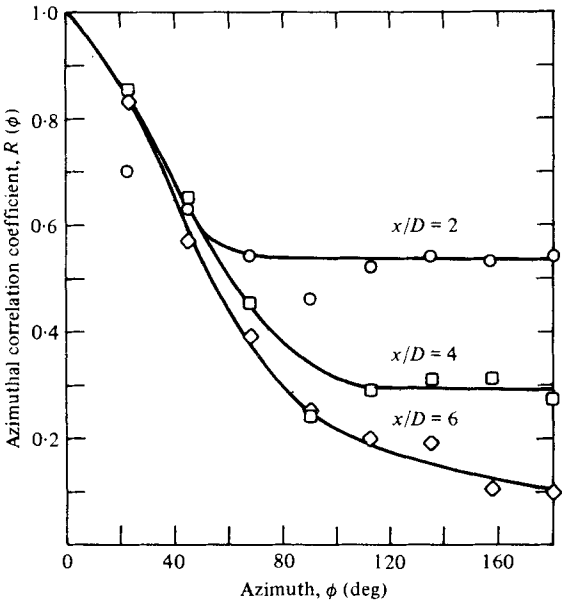

FIGURE 14. Azimuthal variation of correlation coefficient.

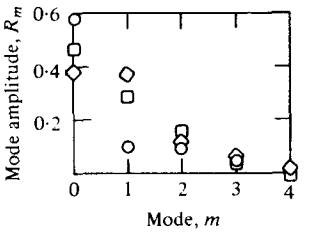

FIGURE 15. Decomposition of azimuthal correlations into modes: $R(\phi) = \Sigma R_m \cos(m\phi)$. ○, $x/D = 2$; □, $x/D = 4$; ◇, $x/D = 6$.

statistical sense, the visualization exhibits some variation in orientation. By $x/D = 4$ the rings occasionally tilted so much that the jet appeared to be locally sinuous, and by $x/D = 6$ the tilting was so extreme that the jet appeared to be sinuous for a good part of the time. Note that at six diameters the jet was nearly as coherent circumferentially as at two diameters, although the large degree of random azimuthal distortion would result in misleadingly small cross-correlation coefficients.

To underline the last point, the variation of the cross-correlation coefficient $R(\phi)$ with azimuth ϕ is plotted in figure 14 for the three axial locations. The azimuthal correlations were decomposed into circumferential modes according to the Fourier series

$$R(\phi) = \sum_{m=0}^{\infty} R_m \cos(m\phi). \tag{3.1}$$

The resulting distribution of the first four modes is shown in figure 15. Notice that by $x/D = 6$ the cross-correlations suggest that there was as much energy in the $m = 1$ (helical) mode as in the $m = 0$ (axisymmetric) mode. However, on the basis of the near-field visualizations this can be accounted for by random straining of vortex structures that were basically ring shaped.

4. Influence of wave dispersion on vortex coalescence

From the previous section it appears that, although the turbulent structures suffer random straining that increases in magnitude with downstream distance, they remain ring shaped at least until the end of the potential-core region. We characterize the rings as annular concentrations of vorticity whose motion is self-induced. Coalescences between adjacent rings are mutually induced by virtue of their compact vorticity, and can be idealized in terms of axisymmetric pairings between potential vortex rings.

The essential feature of the proposed model for the vortex coalescences is a resonant interaction between the vortex structures and a small amplitude subharmonic wave. In order to investigate the model it is necessary to know both the local convection speed of the nonlinear vortex structure and the local phase speed of the linear subharmonic disturbance. The convection speed of the vortex was measured directly from its near-field pressure signature or from flow visualization. The local phase speed of the subharmonic wave was estimated from parallel stability theory. We recognize that a theory that assumes a weakly perturbed laminar flow field may be a poor approximation to a fully developed turbulent mixing layer. However Crighton &

Gaster (1976) have demonstrated that the local dispersion relations obtained from parallel stability theory, as well as the dispersion relation they obtained from their own non-parallel analysis, agree closely with the dispersion measurements made by Crow & Champagne (1971) in a fully turbulent jet that had been forced. These results have been corroborated recently by Moore (1977), who measured wave dispersion in a jet forced at much lower levels than that of Crow & Champagne. By implication, stability eigenvalues are not particularly sensitive to details of the velocity profile, and provide a reasonably good engineering approximation even for a turbulent mixing layer.

4.1. *Spatial stability theory*

The results of two stability analyses are considered. The theories of Michalke (1971) and Mattingly & Chang (1974) both model the jet mixing layer as a laminar annulus with a prescribed velocity distribution. The annulus is disturbed by travelling wave trains of the form

$$\begin{Bmatrix} u_x \\ u_r \\ u_\phi \\ p \end{Bmatrix} (x, r, \phi, t) = \begin{Bmatrix} \hat{u}_x \\ \hat{u}_r \\ \hat{u}_\phi \\ \hat{p} \end{Bmatrix} (r) \exp\left[i(\alpha x + m\phi - \omega t)\right]. \tag{4.1}$$

The variables u_x, u_r and u_ϕ are respectively the axial, radial and azimuthal components of the velocity perturbations and p is the pressure perturbation. The parameters α, m and ω are respectively the wavenumber, azimuthal mode number and frequency of the travelling wave. As the stability analyses are spatial theories, the wavenumber α is complex.

Since the eigenvalues are not sensitive to details of the velocity profile, the particular profile can be characterized by a single parameter, namely its thickness. The eigenvalue solutions can then be applied locally to an arbitrary shear layer by matching the thickness parameter. Michalke's (1971) analysis was based on a hyperbolic-tangent profile, and he chose the momentum thickness θ as the parameter. The analysis of Mattingly & Chang (1974) was based on a half-Gaussian profile, and they chose the parameter $r_{0.5}$, which was defined to be the local jet half-width ($1 > U(r)/U_e > 0.5$). The use of a half-Gaussian profile for the velocity introduced some artificiality into their analysis in that their mean flow coupling term

$$r \frac{d}{dr}\left[\frac{1}{r}\frac{dU(r)}{dr}\right]$$

made its largest contribution at the edge of the shear layer rather than in the centre. Again, since the eigenvalues are insensitive to the velocity profile, this is probably not too serious a limitation.

The mixing layers of turbulent jets grow linearly. The measured thickness parameters for the present air jet were

$$r_{0.5} = 0.105x, \quad \theta = 0.034x. \tag{4.2}$$

The stability eigenvalues were applied to the air jet by selecting the eigenvalue relations that corresponded to the local mixing-layer thickness $\theta(x)$ or $r_{0.5}(x)$. The dispersion curves that appeared as figure 7 in Michalke (1971) are replotted here as figure 16, with the Strouhal time scale based on the exit velocity and diameter. The

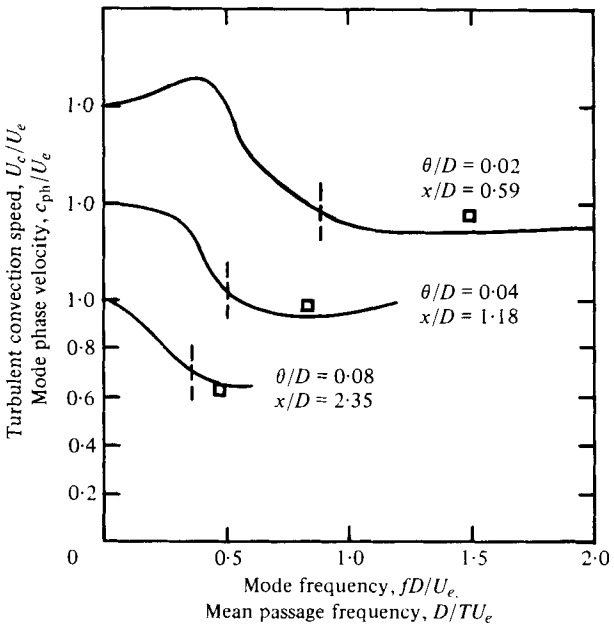

FIGURE 16. Near-field pressure measurements compared with dispersion relations from linear stability theory. ——, dispersion relationship (Michalke 1971); □, pressure measurements.

values of the associated momentum thickness θ/D are indicated alongside the axial locations. Note that the shear layer is dispersive to long waves and relatively non-dispersive to short waves. The latter have phase speeds of about half the jet velocity. Moreover, as the shear layer thickens with downstream distance, it becomes non-dispersive to increasingly longer waves. The wavelength of the longest non-dispersive wave within each dispersion curve is rather subjective. In order to introduce some objectivity into the choice of a dividing frequency, we adopted that of the most amplified waves (indicated in the figure by vertical dashed lines) since they occurred near the lowest non-dispersive frequency.

The open symbols in figure 16 denote mean passage frequencies and convection speeds of the large-scale structures measured from their near-field pressure signatures. The passage frequencies were derived from the zero-counting statistics (figure 9) and the convection speeds from the two-point cross-correlations (figure 3). At each downstream location, the near-field measurements fall near the local dispersion curve and within the non-dispersive range. Moreover the mean near-field passage frequency was roughly an octave above the dividing frequency. Consequently a subharmonic disturbance would have a phase speed nearly equal to the convection speed of the vortex structure.

Loci of dividing frequencies, as defined in figure 16, are plotted in figure 17 as a function of downstream distance. The solid curve was based on the Michalke theory while the broken curve was based on Mattingly & Chang. Together the loci define a dispersive boundary. Waves in the region below the curves are locally dispersive. The near-field passage frequencies were replotted alongside the dispersion boundary. The measurements generally exhibited the same linear trend with x/D as did the curves.

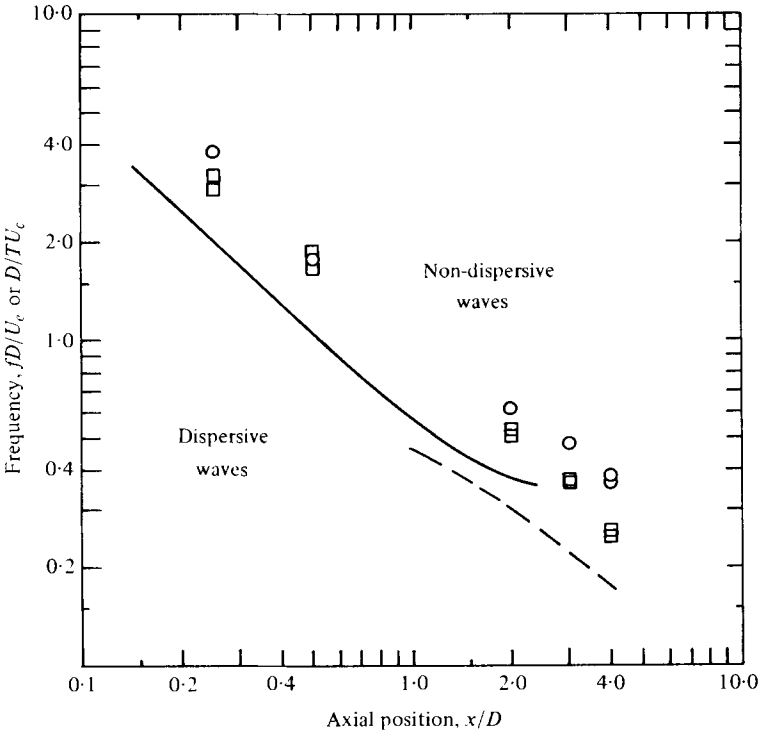

FIGURE 17. Near-field time scales compared with evolution of dispersion boundary. ——, linear eigenmode (Michalke 1971); – – –, linear eigenmode (Mattingly & Chang 1974); ○, most probable near-field passage frequency; □, mean near-field passage frequency.

Most important, the passage frequencies, especially the most probable passage frequencies, fell about an octave above the curves.

Although the octave separation between the vortex passage frequencies and the dispersive boundary is consistent with the subharmonic resonance criterion, it does not necessarily imply a causal relationship. It may imply only that both quantities vary linearly with x/D. A much stronger case can be made by examining the first pairing. As is evident from figure 9, the near-field passage frequency remained constant with x/D until the first vortex pairing had been completed, somewhere between 0·25 and 0·5 diameters downstream. The shear layer became thicker with downstream distance owing to entrainment and vortex roll-up. From figure 17 it is apparent that the first pairing did not occur until the mixing layer was sufficiently thick that it could support a non-dispersive subharmonic disturbance. By inference, the phase locking of the subharmonic was a necessary condition for the pairing to proceed.

The requisite phase locking between quasi-periodic large-scale structures and subharmonic disturbances provides a mechanism for decoupling from the initial conditions. The eigenmode of the initial, laminar instability necessarily increases as the square root of the Reynolds number. However, the dispersive nature of the mixing layer associates each initial vortex spacing with a unique shear-layer thickness that must be attained before adjacent vortices can coalesce. Once the first coalescence has occurred, each successive coalescence doubles the mixing-layer thickness, making it non-dispersive with respect to the next smaller subharmonic frequency.

4.2. *Jet forcing with flow visualization*

A disturbing aspect of the previous section is that the resonance model is deterministic, while the air-jet measurements supporting the model were entirely statistical. The reason for this is, of course, the statistical variation of local conditions, which is induced in large part by spatial variance in the location of vortex coalescences.

Local variations can be reduced by forcing the jet. Superimposing a small periodic surging on the flow field has the effect of spatially localizing coalescences between vortices whose passage frequency matches the surging. When the jet structure is regularized in this way, local conditions become periodic, permitting ensemble-averaged measurements to describe instantaneous conditions accurately.

The forced-jet measurements were made with the water-jet facility operating at Reynolds numbers of 5000, 10000, 20000 and 40000. At each Reynolds number, the jet was forced at Strouhal numbers of 0·5, 1·0, 1·5 and 2·0. Dye visualization was used to measure the spacing between the vortex rings and to determine the location of the pairings. The photographs in figure 18 (plate 1) show the jet forced near $St = 1$ at two different Reynolds numbers. The jet was illuminated by a strobe flashing in synchronization with the forcing. Each photograph was a multiple-exposure photograph taken over a number of flashes. The technique selected periodic motion that was phase locked with the forcing. The effectiveness of forcing in localizing the occurrence of a vortex pairing is best illustrated at low Reynolds number (figure 18*a*). The photograph, which was an ensemble of 10 strobe exposures, repeatedly captured two vortex rings undergoing a pairing at a fixed point in space. Once the pairing was complete, the spacing between rings had doubled and, by conservation of waves, the passage frequency had been halved. This frequency halving can be immediately recognized from the reduced exposure. The rings spaced periodically downstream of the pairing in figure 18(*a*) are lighter because they were present in only every other strobe exposure. Further downstream in the same photograph a second pairing not phase locked by the forcing destroyed the phase reference. The multiple-exposure visualizations were substantially the same at higher Reynolds number (figure 18*b*), although the details of the flow were not as well ordered. In any case, the completion of the first pairing was located in the photograph to within a fraction of a wavelength by noting the onset of reduced exposure and loss of phase reference.

Vortex convection speeds were also deduced from the photographs. The vortex spacings λ/D were measured directly, the passage frequencies were fixed by the forcing, and

$$U_c/U_e = St(\lambda/D). \tag{4.3}$$

The results are plotted in figure 19 for the range of Reynolds numbers. The vortex rings travelled at roughly 60 % of the jet velocity, independent of the forcing frequency or Reynolds number.

The range of forcing frequencies, $St = 0{\cdot}5$–2, was deliberately chosen to include Strouhal numbers smaller than the lowest non-dispersive frequency supported by the initial shear layer. In practice, though, it was not possible to excite vortex rings that moved faster than $0{\cdot}6U_e$. When the forcing frequency was slightly below the non-dispersive limit, small amplitude waves were excited that travelled faster than $0{\cdot}6U_e$. By the point where the roll-up was complete, however, the shear layer was thick enough that the forced disturbance was locally non-dispersive. When the initial

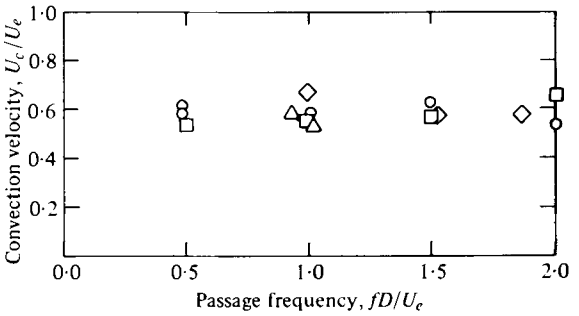

FIGURE 19. Convection speeds of vortex rings at different forcing frequencies. Reynolds number: ○, 5000; □, 10000; ◇, 20000; △, 40000.

shear layer was driven an octave or more below its lowest non-dispersive frequency, the resulting instability was driven by harmonics of the forcing rather than by the forcing frequency itself. This sort of harmonic coupling is shown in figure 20 (plate 2). This is a multiple-exposure photograph, illuminated by a strobe synchronized to the forcing. The jet was operated at a Reynolds number of 5000 and driven at a Strouhal number of 0·48, which was about an octave below the lowest non-dispersive frequency based on the initial shear-layer thickness. Two sets of vortex spacings are apparent in the figure, both phase locked to the forcing. The first set was created by the linear instability and had a passage frequency of $St = 1{\cdot}0$, the first harmonic of the forcing. At a fixed position downstream, the first set of rings paired with each other, resulting in the second set of rings, which has twice the spacing and half the frequency (i.e. $St = 0{\cdot}5$, the forcing frequency). Moreover, the second set of rings, whose passage frequency matched the forcing, was particularly stable with respect to subsequent pairings. The next pairing was delayed until a point beyond four or five diameters downstream. In the space between pairings, as is evident from the plate, the growth of the mixing layer was inhibited. This behaviour is expressed quantitatively in figure 21, which was measured by Browand (1976, private communication) in the same water jet. The flow was visualized with dye, and through frame-by-frame analysis of a high-speed motion picture, vortex passage times were noted at eight axial positions and median passage frequencies calculated. The figure displays the median passage frequencies *vs.* axial location for a family of forcing frequencies, as well as for an unforced case. When the jet was forced at frequencies near or above the natural instability ($St = 1{\cdot}2$), the instability was driven by the forcing and the passage frequency decreased smoothly with downstream distance, reaching a Strouhal number of 0·5 at around four diameters. When the jet was forced at the first and second subharmonics of the natural instability, the instability was not driven at the forcing frequency. Instead it was driven at high, non-dispersive harmonics of the forcing frequency and the passage frequencies decreased with downstream distance in discrete jumps, corresponding to phase-locked pairings, until the forcing frequency was attained. Once that frequency was attained the vortices were quite stable, with no further pairings until beyond four diameters.

The mean locations of the pairings were deduced from figure 21 by applying conservation of waves. Where a pairing has been completed half the vortices will have disappeared, halving the passage frequency. The deduced locations of completed pairings

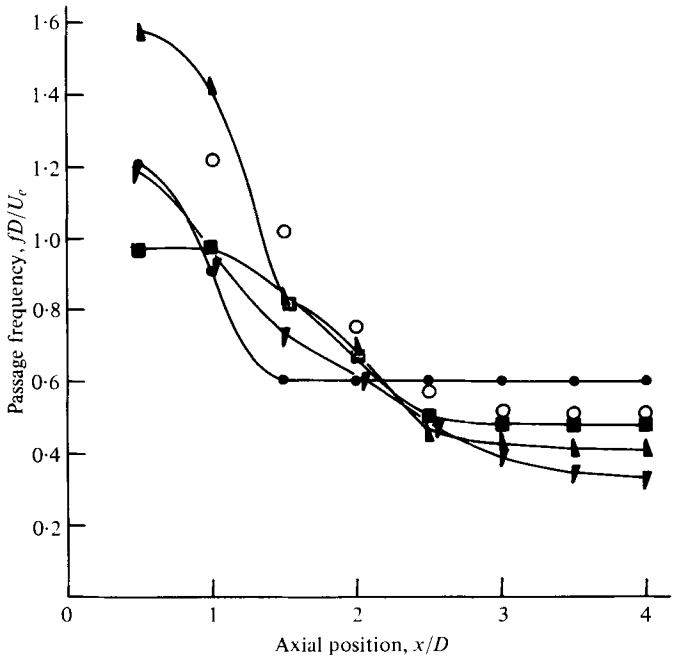

FIGURE 21. Axial variation of mean vortex passage frequencies in forced water jet (Browand 1976, private communication). Reynolds number = 5000. Strouhal number of forcing: ▲, 1·6; ■, 1·0; ●, 0·6; ▼, 0·3; ○, no forcing.

are plotted in figure 22 as a function of the subharmonic, paired frequencies resulting. The pairing locations estimated from the multiple-exposure photographs are plotted for comparison, as are pairing locations estimated from the free air jet by applying conservation of waves to the measured mean passage frequencies (figure 11). There is general agreement between pairing locations estimated by the two different methods and for the two different jets. Moreover, there is no obvious viscous influence over the range of Reynolds numbers considered. The pairing location generally varies inversely with the resultant subharmonic.

In an investigation of local influences on vortex interaction using different jets operated at different Reynolds numbers and with different initial conditions, the local mixing-layer thickness, rather than axial position, is a more relevant scaling parameter. As was evident in figure 20, forcing can significantly alter the mixing-layer growth. So, in order to measure correctly the mixing-layer thickness at the location of a pairing, it is important that the jet is being forced during the measurement. Again a photographic technique was devised, based on multiple exposures. The jet was operated at the same Reynolds numbers and forced at the same Strouhal numbers as in the dye photographs. The mixing-layer growth was visualized using pulsed hydrogen bubbles illuminated by a stroboscope. This time, however, the strobe was synchronized to the bubble-wire pulsing, rather than to the jet forcing. The bubble pulses maintained their phase relative to the wire as they propagated through parallel flow regions, but the phase reference was destroyed in regions where there was mixing. In this way, the boundaries of the mixing layer were marked visually. Figure 23 (plate 2) is a typical visualization. The initial conditions were the same as

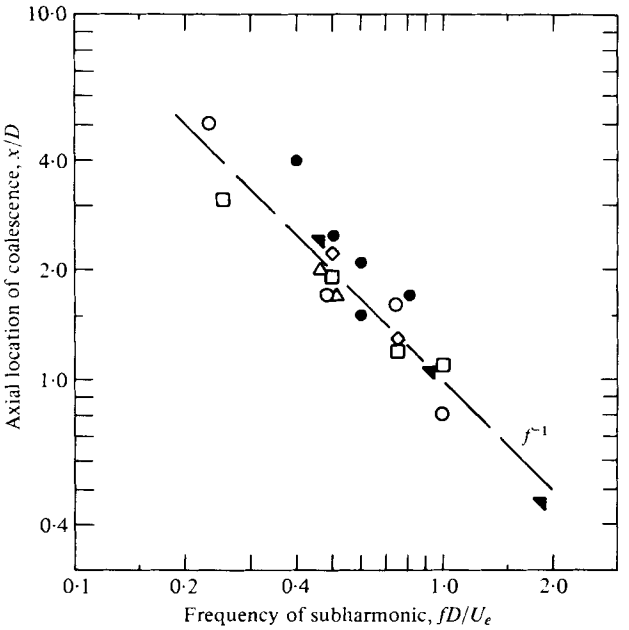

FIGURE 22. Axial location of successive coalescences plotted against resulting 'subharmonic'. Reynolds number: ○, 5000; □, 10000; ◇, 20000; △, 40000; ◥, 52000 (air jet); ●, 5000 (Browand 1976, private communication).

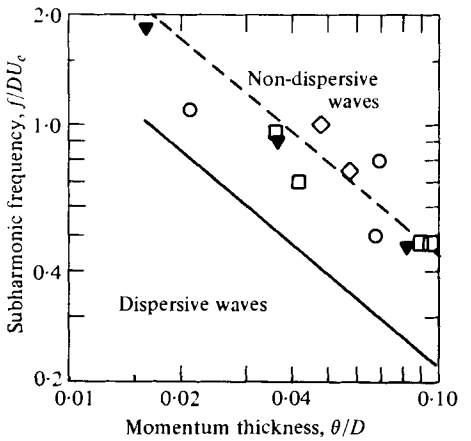

FIGURE 24. Local momentum thickness after vortex coalescence plotted against resulting 'subharmonic'. ——, dispersion boundary; – – –, parallel line one octave above dispersion boundary. Reynolds number: ○, 5000; □, 10000; ◇, 20000; ▼, 52000 (air jet).

for figure 20, namely $Re = 5000$ and $St = 0{\cdot}48$. The growth of the mixing layer is clearly visible and its thickness can be measured directly from the photograph at any axial position within the first few diameters.

Information from the two sets of flow visualizations is cross-plotted in figure 24. For each forcing frequency, the axial position where the first pairing was complete was determined from the dye photographs and plotted against the paired, subharmonic

frequency in figure 22. With the pairing location known, the corresponding mixing-layer thickness was measured from the hydrogen-bubble photographs. The momentum thickness was assumed to be 20 % of the velocity-profile thickness. In figure 24 the subharmonic frequency is cross-plotted against the momentum thickness θ/D measured at the completion of the pairing. The pairing locations in the free air jet deduced from conservation of waves are also cross-plotted for comparison. The dispersion boundary is plotted alongside the measurements. A dashed line is plotted an octave above the dispersion boundary and although there is considerable scatter this dashed line passes through the data. Consequently, a wave disturbance with a wavelength twice the spacing of the paired vortices would have a phase speed that matched the convection speed of the vortices.

5. Conclusions

(i) For an incompressible air jet operated at moderate Reynolds number, the dominant turbulent structure was a ring of concentrated vorticity. These structures were statistically axisymmetric and were spaced quasi-periodically. Individual realizations of the mixing layer, derived from an azimuthal microphone array, suggested that the rings experienced distortions in orientation, which increased in magnitude with downstream distance. At some point beyond the end of the potential core, the semblance of axisymmetry had disappeared and the jet appeared sinuous much of the time.

(ii) Detailed examination of the 'visualizations' derived from the azimuthal microphone array suggested that over the range 2–6 diameters downstream there was relatively good coherence around the jet. However, random straining created the appearance of poor azimuthal coherence when averages over time were taken.

(iii) Estimates of the passage frequency of the large-scale structures past a point in space were derived from their signatures in the hydrodynamic near field of the jet. Depending upon how the time scale was defined, however, estimates derived from the same data base varied over as much as an octave (figure 11). Generally speaking, the most probable passage period, as derived from zero-crossing statistics, produced the largest estimated passage frequency. This was followed in order by the estimate based on the autocorrelation period, the estimate based on the mean passage period (derived from zero-crossing statistics), and finally, the frequency of the power spectral peak.

(iv) Air- and water-jet measurements were combined to examine the relationship between vortex pairings and the local mixing layer. Evidence was presented (figure 24) to show that over a reasonably wide range of Reynolds numbers the local thickness of the mixing layer at the completion of a pairing scaled with the passage frequency of the paired vortices.

(v) A model was suggested that could account for the scaling of vortex pairing with mixing-layer thickness. A vortex pairing was idealized as a resonant interaction between a set of vortex rings and a linear subharmonic disturbance. The interaction depends on the linear dispersion of the local mixing layer. Parallel stability theory was used to estimate the local dispersion relation as a function of downstream distance. Measurements were presented which suggested that the first pairing occurred where the mixing layer became sufficiently thick, owing to nonlinearities and entrainment,

that a subharmonic wave had a phase velocity that matched the convection speed of the vortex rings.

The author would like to thank Professors J. Laufer, F. K. Browand and R. E. Kaplan for their comments and technical guidance. Thanks are also due to Ms Mary Vassilakis for her assistance with the flow-visualization experiments. The support of the National Aeronautics and Space Administration under grant number NSG-1221 is gratefully acknowledged.

REFERENCES

ANDERSON, A. B. C. 1955 Structure and velocity of the periodic vortex-ring flow pattern of a pipe tone jet. *J. Acoust. Soc. Am.* **27**, 1048–1052.

BRADSHAW, P., FERRISS, D. H. & JOHNSON, R. F. 1964 Turbulence in the noise-producing region of a circular jet. *J. Fluid Mech.* **19**, 591–624.

BROWAND, F. K., CHU, W. T. & LAUFER, J. 1975 Exploratory experiments on the entrance effects in subsonic jet flows. *Dept. Aero. Engng, Univ. Southern Calif. Rep.* no. 130.

BROWAND, F. K. & LAUFER, J. 1975 The role of large scale structures in the initial development of circular jets. *Proc. 4th Symp. Turbulence in Liquids, Univ. Missouri–Rolla.*

BROWAND, F. K. & WEIDMAN, P. D. 1976 Large scales in the developing mixing layer. *J. Fluid Mech.* **76**, 127–144.

BROWN, G. & ROSHKO, A. 1971 The effect of density differences on the turbulent mixing layer. *Turbulent Shear Flows, AGARD Current Paper*, no. 93, pp. 23.1–23.12.

BROWN, G. & ROSHKO, A. 1974 On density effects in turbulent mixing layers. *J. Fluid Mech.* **64**, 775.

CRIGHTON, D. G. & GASTER, M. 1976 Stability of slowly diverging jet flow. *J. Fluid Mech.* **77**, 397–413.

CROW, S. C. & CHAMPAGNE, F. H. 1971 Orderly structure in jet turbulence. *J. Fluid Mech.* **48**, 547–591.

DAVIES, P. O. A. L., FISHER, M. J. & BARRATT, M. J. 1963 The characteristics of the turbulence in the mixing regions of a round jet. *J. Fluid Mech.* **15**, 337–367.

DOMM, U. 1956 Uber eine Hypothese, die den Mechanismus der Turbulenz–Enstehung betrifft. *Dsche Versuchsanstalt Luftfahrt (DVL) Rep.* no. 23.

FUCHS, H. V. 1972 Measurements of pressure fluctuations within subsonic turbulent jets. *J. Sound Vib.* **22**, 361–378.

FUCHS, H. V. 1974 Resolution of turbulent jet pressures into azimuthal components. *AGARD Conf. Proc.* no. 131, paper 27.

KO, N. W. M. & DAVIES, P. O. A. L. 1971 The near field within the potential core of subsonic cold jets. *J. Fluid Mech.* **50**, 49–78.

KONRAD, J., ROSHKO, A. & BROWN, G. L. 1976 The development of three dimensionality and the extent of the molecular mixing in a turbulent shear flow. *Bull. Am. Phys. Soc., Div. Fluid Dyn.* no. 21, paper CB2.

LAU, J. C., FISHER, M. J. & FUCHS, H. V. 1972 The intrinsic structure of turbulent jets. *J. Sound Vib.* **22**, 379–406.

LAUFER, J. 1974 On the mechanism of noise generation by turbulence. *Omaggio a Carlo Ferrari* (ed. Levrotto & Bella), pp. 449–464.

LAUFER, J., KAPLAN, R. E. & CHU, W. T. 1974 On the generation of jet noise. *AGARD Conf. Proc.* no. 131, paper 21.

MATTINGLY, G. E. & CHANG, C. C. 1974 Unstable waves on an axisymmetric jet column. *J. Fluid Mech.* **65**, 541–560.

MICHALKE, A. 1971 Instabilität eines Kompressiblen runden Freistrahls unter Berücksichtigung des Einflusses der Strahlgrenzschichtdicke. *Z. Flugwiss.* **19**, 319–328.

MICHALKE, A. & FUCHS, H. V. 1975 On turbulence noise of an axisymmetric shear flow. *J. Fluid Mech.* **70**, 179–205.

MOLLO-CHRISTENSEN, E. 1967 Jet noise and shear flow instability seen from an experimenter's viewpoint. *Trans. A.S.M.E., J. Appl. Mech.* **34**, 1–7.

MOORE, C. J. 1977 The role of shear-layer instability waves in jet exhaust noise. *J. Fluid Mech.* **80**, 321–367.

PATNAIK, P. C., SHERMAN, R. S. & CORCOS, G. M. 1976 A numerical simulation of Kelvin–Helmholtz waves of finite amplitude. *J. Fluid Mech.* **73**, 215–240.

SIDDON, T. E. 1969 On the response of pressure measuring instrumentation in unsteady flow. *Univ. Toronto UTIAS Rep.* no. 136.

TOWNSEND, A. A. 1956 *The Structure of Turbulent Shear Flow.* Cambridge University Press.

WINANT, C. D. & BROWAND, F. K. 1974 Vortex pairing: the mechanism of turbulent mixing-layer growth at moderate Reynolds number. *J. Fluid Mech.* **63**, 237–255.

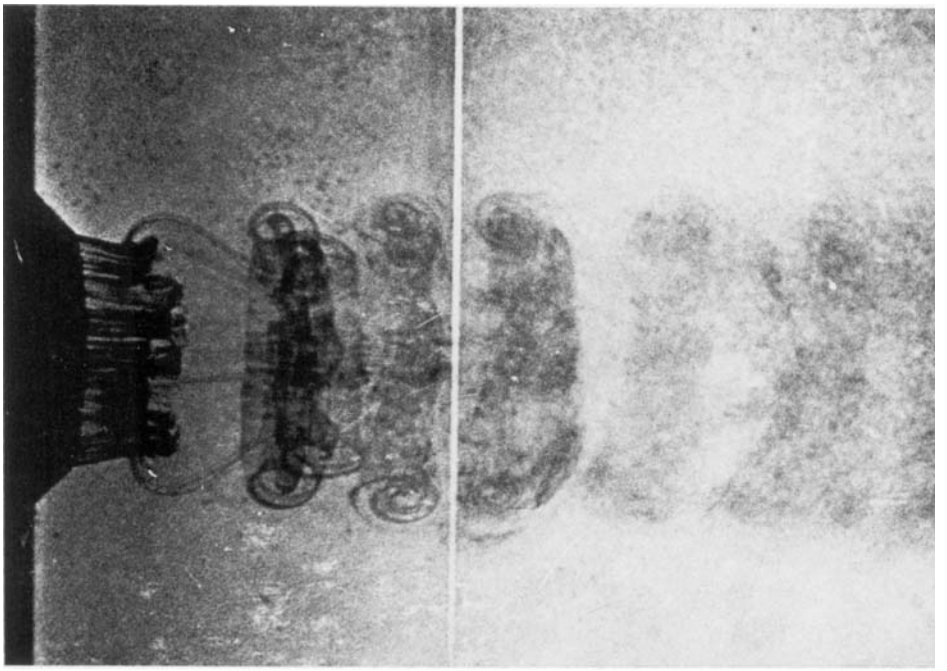

(*a*)

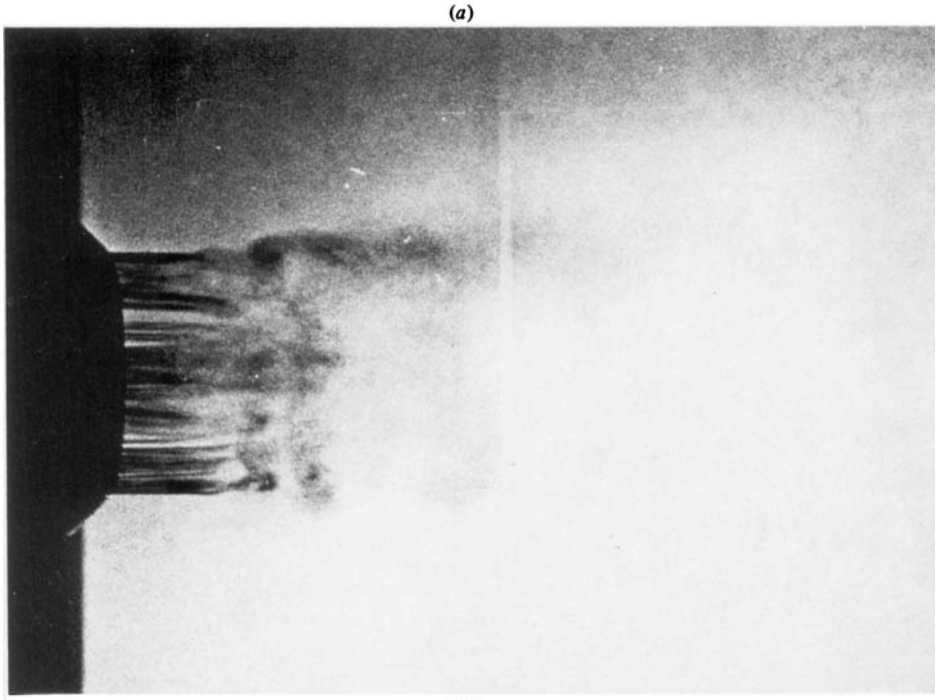

(*b*)

FIGURE 18. Dye visualization of water jet being forced at Strouhal number of 1·0. (*a*) Reynolds number = 5000; (*b*) Reynolds number = 20000.

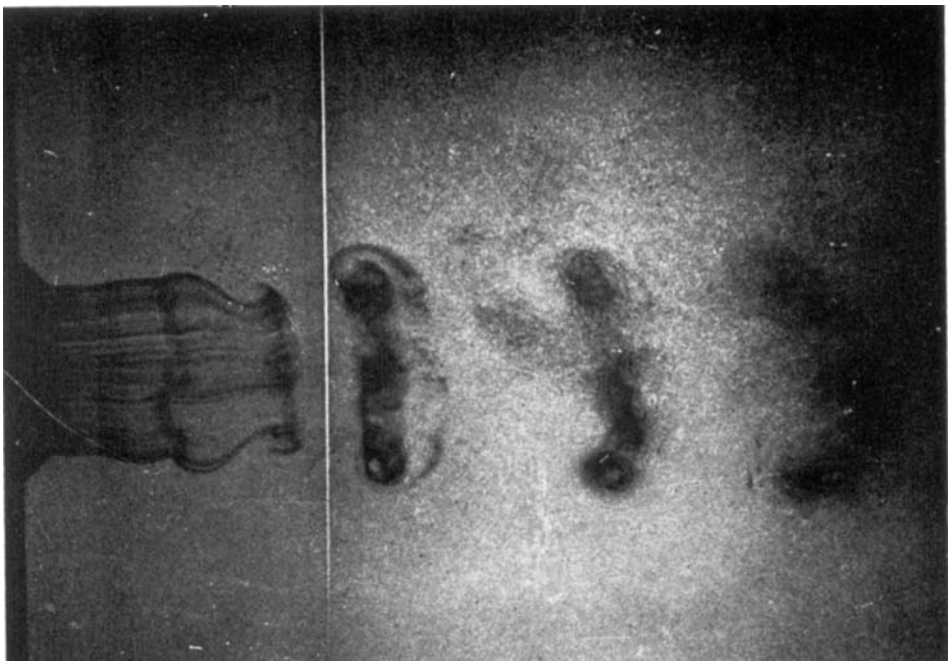

FIGURE 20. Dye visualization of water jet being forced at $St = 0{\cdot}48$; Reynolds number = 5000.

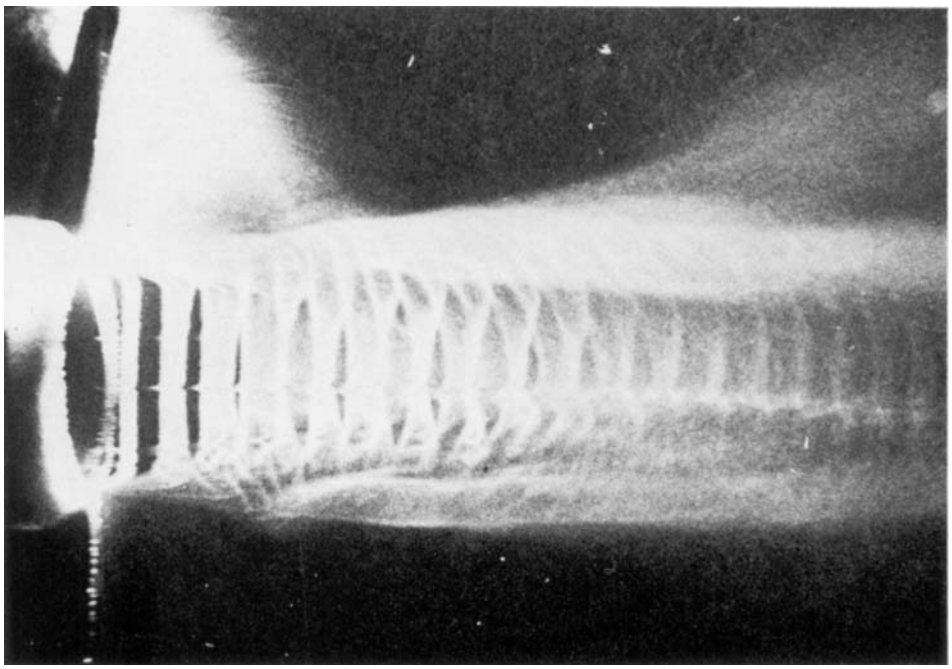

FIGURE 23. Hydrogen-bubble visualization of water jet being forced at $St = 0{\cdot}48$; Reynolds number = 5000.